PHYSICAL REVIEW B **83**, 085411 (2011)

Interplay between structure and electronic states in step arrays explored with curved surfaces

J. E. Ortega,[1,2,3] M. Corso,[3] Z. M. Abd-el-Fattah,[2] E. A. Goiri,[3] and F. Schiller[2]
[1] *Universidad del País Vasco, Departamento Física Aplicada I, E-20018 San Sebastián, Spain*
[2] *Centro de Física de Materiales, Consejo Superior de Investigaciones Científicas (CSIC)/Universidad del País Vasco-Euskalherriko Unibertsitatea (UPV/EHU)-Material Physics Center, Manuel Lardizabal 5, E-20018 San Sebastián, Spain*
[3] *Donostia International Physics Center, Paseo Manuel Lardizabal 4, E-20018 Donostia-San Sebastián, Spain*

(Received 7 December 2010; published 14 February 2011)

Atomic staircases in noble-metal surfaces are model one-dimensional superlattices, where free-electron-like surface states transform into superlattice bands with sizable quantum size shifts and gaps. At critical step spacings $d = n \times (\lambda_F/2)$, such superlattice gaps lie at the Fermi energy, affecting the electronic energy and hence the structural stability of the step lattice, which is held by weak elastic interactions. We use Cu, Ag, and Au curved crystals to smoothly tune the superlattice constant d in angle-resolved photoemission (ARPES) and scanning tunneling microscopy (STM) experiments. With ARPES we accurately quantify terrace-size effects and determine the superlattice potential, which increases from Ag to Cu and to Au. With STM we analyze the d-dependent terrace width distribution for Cu and Ag, and observe nonlinear variations in Cu. On the grounds of simple electronic and elastic models, we conclude that terrace width distribution instabilities and electronic energy variations at $d = n \times (\lambda_F/2)$ have the same order of magnitude for Cu. In contrast, the weak superlattice potential in Ag, i.e., its smoother band-structure modulation, is not sufficient to alter the step lattice.

DOI: 10.1103/PhysRevB.83.085411 PACS number(s): 73.20.At, 73.22.−f

I. INTRODUCTION

Metallic superlattices, such as atomic step arrays, are actively investigated in the context of nanostructure growth, as suitable templates to achieve self-organized, dense nanoparticle arrays with 1–10 nm periodicities.[1] At this length scale, long-range interactions, namely, elastic, dipole, and substrate-electron-mediated interactions, compete to determine the equilibrium structure in templates and arrays. Understanding the hierarchy of such interactions is thus of obvious importance. To this aim, step lattices are particularly attractive because they are the simplest one-dimensional (1D) systems. The nanoscale order in a step lattice is driven by long-range, elastic repulsion between steps.[1,2] Compared to atomic bonds, such elastic interactions are weak, and hence the 1D superlattice is likely to be influenced by surface electronic states. In particular, in noble metals, where surface electrons scatter strongly at crystal defects, such as steps, giving rise to a significant $2k_F$ ($\lambda_F/2$) response at the Fermi energy.[3–6] The question that arises is whether surface electron scattering in step arrays is enough to trigger 1D charge-density-wave-like phenomena, i.e., structural-electronic instabilities with a lattice constant (step spacing) $d = n \times \lambda_F/2$.

The existence of electronic-structural interplay associated to surface states on noble metals has been shown for adatoms and molecules adsorbed at cryogenic temperatures.[3] In the most striking case, Ce adatoms form a hexagonal lattice on Ag(111) with parameter d that matches the surface-state Fermi wavelength $\sim \lambda_F/2$, leading to the so-called nesting of the Fermi surface with superlattice wave vectors. However, adatom lattices are delicate systems that become unstable at room temperature, and hence have little interest for applications. In dislocation patterns and arrays of steps electronic-structural instabilities have been claimed at 300 K.[7,8] In the dislocation network induced by one monolayer of Ag on Cu(111), the two-dimensional (2D) Fermi surface nesting and subsequent gapping may explain the extra compression observed in the Ag atomic lattice.[7] In step arrays in vicinal Cu(111), the Fermi surface gap is observed with $d = \lambda_F/2$, where a disorder instability is invoked, but not proved.[8]

In order to test the existence of electronic-structural interplays, superlattices with a tunable lattice constant are extremely useful. For step arrays, the tunability is readily achieved with curved surfaces. In this work we present a combined analysis of the structure and the electronic states of tunable Cu and Ag step superlattices using curved crystals. A similar analysis was previously done for Au, and presented elsewhere.[9] As shown in Figs. 1(a) and 1(b), our curved surfaces are defined by $\alpha = \pm 15^\circ$ cylindrical sections around the [111] direction ($\alpha = 0$). The 1D superlattice is thus made of monatomic steps that run parallel to the $[1\bar{1}0]$ direction, whereas along $[11\bar{2}]$ the superlattice constant d is inversely proportional to the macroscopic deviation (α) from the [111] direction as

$$d = \frac{h}{\sin\alpha}, \tag{1}$$

where h is the monatomic step height. Therefore, d is accurately and smoothly varied by scanning the respective probes along $[11\bar{2}]$, i.e., the micrometer-sized synchrotron light beam in angle-resolved photoemission spectroscopy (ARPES) and the metallic tip in scanning tunneling microscopy (STM). This allows us to measure d-dependent properties directly, such as the surface band structure (Figs. 2 and 3) and the terrace confinement shift (ΔE, Fig. 4) in ARPES, as well as the terrace-size distribution in STM (Figs. 5 and 6). From ΔE we derive the superlattice potential strength $U_0 b$ in Fig. 1(c), which is found to increase from Ag to Cu and Au. Such a trend correlates well with the observation of very strong structural instabilities in Au (faceting), terrace-size distribution variations in Cu, and apparent structural stability in Ag step lattices. Moreover, a quantitative estimation of the structural and the electronic energy variations in each

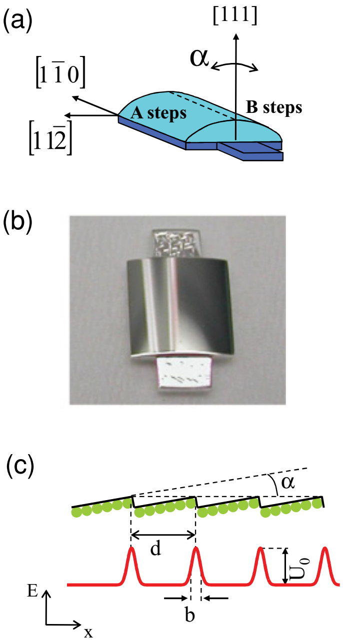

FIG. 1. (Color online) (a) Schematic description of the Au, Cu, and Ag curved crystal samples and (b) photograph of the 6 × 6 mm^2 Ag crystal used in this work. α stands for the miscut deviation with respect to the (111) surface at the center of the crystal. (c) Side-view sketch of the 1D periodic potential in a step superlattice with lattice constant d and $U_0 b$ barriers at step edges.

case supports the existence of a delicate interplay between electronic states and the lattice structure in step arrays of noble metals.

II. EXPERIMENTAL

Ag, Cu, and Au single crystals (Mateck GmbH, Germany) were mechanically polished, defining a $\alpha = \pm 15^\circ$ cylindrical section (11.6 mm radius) around the [111] direction ($\alpha = 0$) [Fig. 1(a)]. Figure 1(b) shows a photograph of the Ag crystal. As depicted in Fig. 1(a), the two sides of the crystal correspond to A-type steps ({100}-oriented microfacets) and B-type steps ($\{11\bar{1}\}$ microfacets). All surfaces were prepared in vacuum following the standard ion sputtering plus annealing cycling used for flat crystals. The small size of the sample allows a homogeneous preparation for all miscuts, ensuring reliable d-dependent analysis. The low-energy electron diffraction (LEED) scans display smooth and sharp d-dependent splitting across the sample for Cu and Ag.[10] In contrast, the Au crystal exhibited clear faceting in the ∼4°–10° range, as discussed elsewhere.[9]

Locally resolved surface bands were measured with ARPES using synchrotron light from the Plane Grating Monochromator beamline of the Synchrotron Radiation Center (SRC) in Stoughton (Wisconsin, USA). We used a hemispherical Scienta SES200 analyzer with energy and angular resolution set from 25 to 35 meV and 0.1°, respectively, and p-polarized light with the polarization plane parallel to surface steps. The 100-μm-diam light spot defined an effective $\Delta\alpha \sim 0.25^\circ$, i.e., similar to the nominal polishing accuracy of crystals.[9] The samples were mounted with the $[11\bar{2}]$ crystal direction running parallel to the analyzer entrance slit, such that the 1D step superlattice band dispersion could be directly imaged in the channel-plate detector of the analyzer. For line-fit analysis, channel-plate images were decomposed in single energy dispersion curves (EDC) for each of the 127 channels. Peak fits were carried out using two Lorentzian lines for the surface state and its umklapp band convoluted by a Gaussian to account for temperature and experimental resolution. The series of fits determined peak energy, width, and intensity.

The structural quality of the step superlattices as a function of d is defined from the standard deviation of the lattice constant $\sigma(d)$, i.e., the terrace width distribution measured across the curved crystals with STM. Images have been systematically recorded using a variable temperature STM setup (Omicron). The description of the analytical process of the STM images, which is the same for the three crystals, was explained in detail in the previous Au work.[9] In summary, we perform a thorough analysis of individual frames with sizes between 400 × 400 and 20 × 20 nm^2 using the WSXM software.[11] STM images are automatically processed, applying a Gaussian fit to the resulting data that gives the value $\bar{d}$ in each image, as well as the standard deviation σ.[9] The STM analysis is always limited to surface areas exhibiting homogeneous step arrays in the 1-μm scale, i.e., generally most of the surface areas with miscut angles above 2°. For each $\sigma(d)$ point we consider an average of five different frames. Error bars in $\bar{d}$ are estimated as $\Delta\bar{d} = \sqrt{\Delta\bar{d}_a^2 + \Delta\bar{d}_b^2}$, where $\Delta\bar{d}_a$ stands for the numerical precision determined by the fitting program, and $\Delta d_b = h(\cos\alpha/\sin^2\alpha) \times \Delta\alpha$ accounts for the local lattice constant variability derived from the $\Delta\alpha = 0.2^\circ$ accuracy of the surface orientation. Finally, the uncertainty in σ is defined by the fitting program. STM experiments were carried out at 300 K for Cu and Au(111), and at 150 K for Ag, the latter intended to attenuate the effect of bunching of surface steps induced by the STM tip.

III. ARPES: DETERMINING THE SUPERLATTICE POTENTIAL

Figures 2 and 3 display ARPES results for the Cu and Ag curved surfaces, respectively. We show intensity plots showing the surface bands perpendicular to the step arrays in Cu and Ag [Figs. 2(a) and 3(a)], EDC spectra at band minima for different α [Figs. 2(b) and 3(c)], Fermi surfaces [Fig. 2(c)] around the nesting point in Cu ($d = \lambda_F/2 \sim 17$ Å),[8] and also the characteristic photon-energy dependence of the band umklapps in the case of Ag [Fig. 3(b)]. Generally, measurements with two photon energies need to be combined, i.e., a low photon energy of 21 eV, which provides high intensity and optimum energy and angular resolution for an individual EDC peak analysis, and a high photon energy between 33 and 46 eV, to better visualize umklapp bands. The latter are needed to define $2\pi/d$, i.e., the actual terrace size d being probed in the ARPES experiment. In Fig. 2(a) the lines are Kronig-Penney (KP) fits to data (see below), whereas in Fig. 3(a) parabolic fits mark the dispersion near the band bottom. Owing to the proximity of the Fermi level, the surface-state peak in Ag appears convoluted with the Fermi edge, making the band dispersion barely visible in image plots

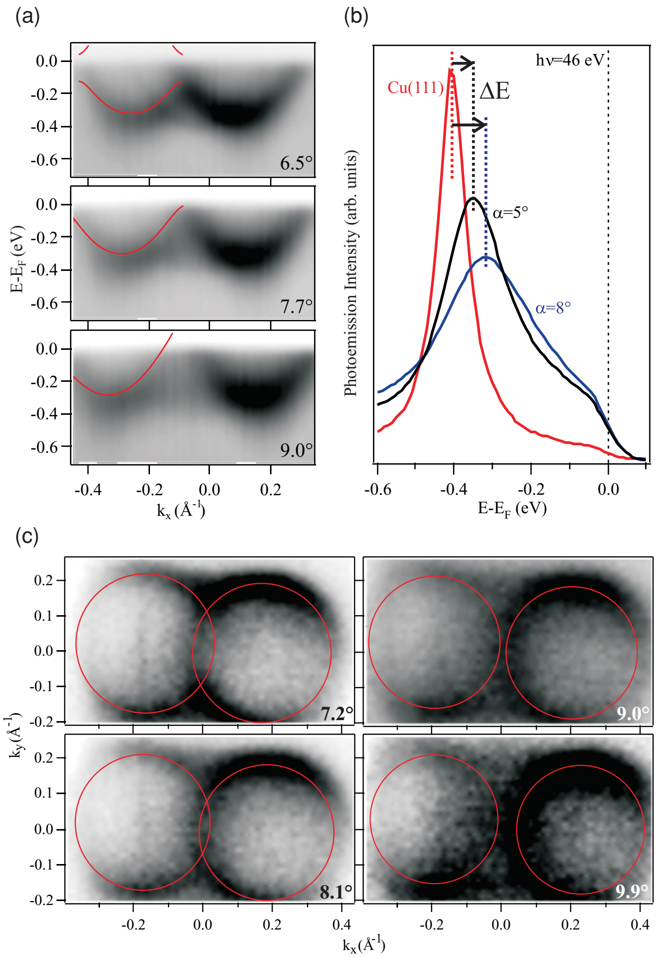

FIG. 2. (Color online) (a) Photoemission intensity plots showing the surface band dispersion measured around $d = \lambda_F/2$ at different miscut angles in curved Cu. The solid lines are KP bands that indicate the presence of a Fermi gap. (b) EDC spectra for band minima at different angles, from which the d-size effect (ΔE) is straightforwardly determined. (c) Photoemission intensity at the Fermi energy for different miscuts in Cu. The rings mark the intensity maxima and hence the Fermi surface. For 7.2° and 8.1° miscuts the intensity weakens at the ring crossing region, indicating the presence of a gap.

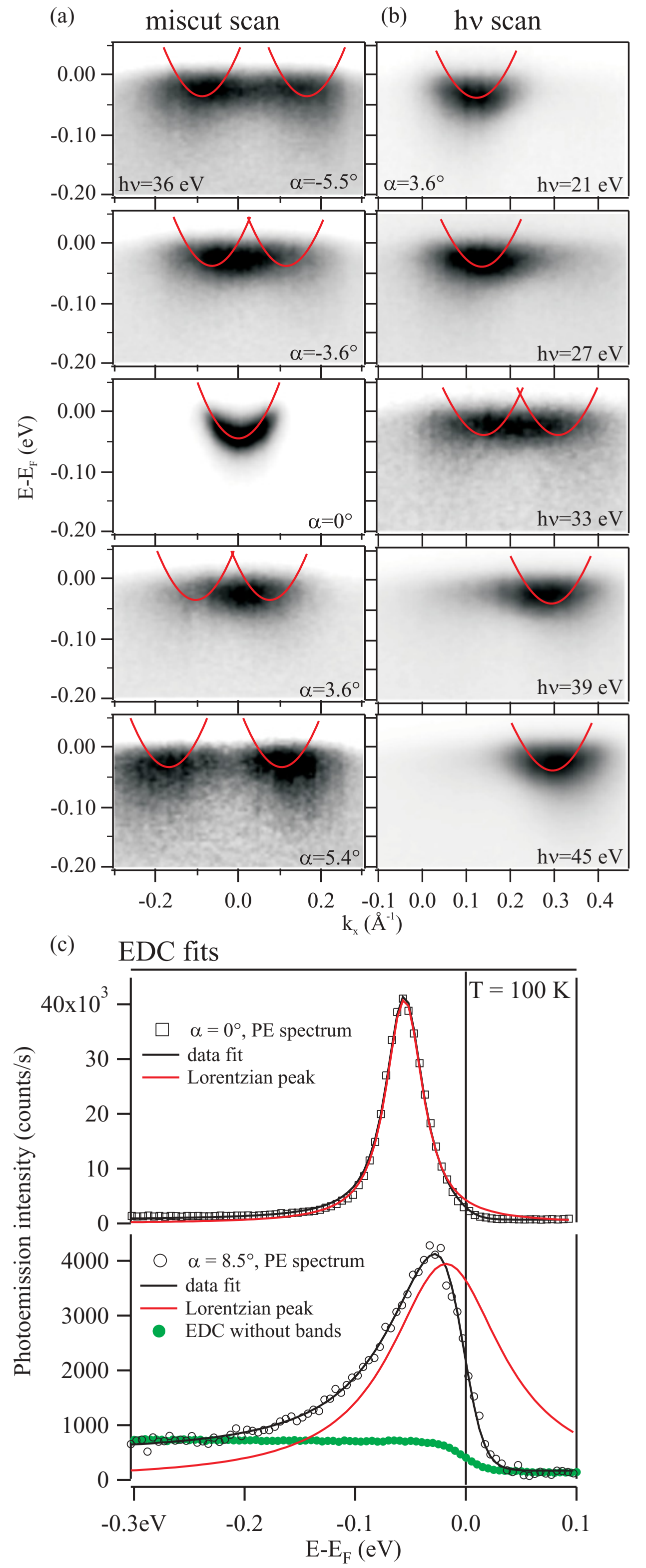

FIG. 3. (Color online) (a) Photoemission intensity plots showing the surface-state band in Ag at different miscut angles. (b) Photon-energy dependence of the surface-state band in Ag at $\alpha = 3.6°$. Umklapps are better observed near the Γ point of the bulk band structure, probed with 33–36 eV photon energy. (c) Surface-state peak fits carried out at surface band minima in curved Ag at $\alpha = 0°$ [(111) surface] and $\alpha = 8.5°$. In the latter, the peak is cutoff by the Fermi edge, which needs to be deconvoluted by line fitting.

such as those of Fig. 3(a). In Fig. 2(c) the umklapp rings mark the intensity maxima at E_F, allowing to identify Fermi surface nesting. In agreement with previous measurements,[8] the intensity drops at the crossing point of the two Fermi rings from 7° to 8° miscuts, reflecting the presence of the Fermi gap around the critical $d = \lambda_F/2 \sim 17$ Å value.

The EDC spectra in Figs. 2(b) and 3(c) correspond to the surface band bottom at different α angles, reflecting the characteristic upward shift (ΔE) of the surface band minimum with respect to the (111) band (E_0). The positive ΔE is the clearest ARPES signature of repulsive step barriers and partial confinement within d-wide terraces. In Ag [Fig. 3(c)] the surface-state peak is cutoff by the Fermi level at high miscut angles, and hence the peak position is only determined after line-fit analysis. Because E_0 is simply measured at the center of each crystal, we can obtain a very consistent and accurate determination of ΔE vs d. In Fig. 4 we show such

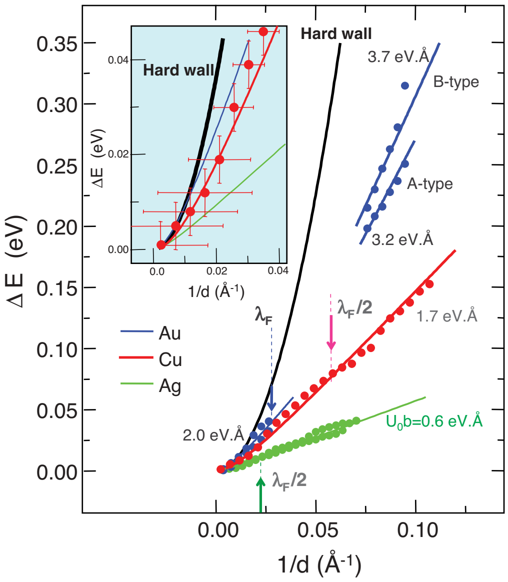

FIG. 4. (Color online) Terrace-size confinement effect for Ag, Cu, and Au step lattices. Solid lines are fits to the respective sets of data using the KP model to extract the step barrier strength U_0b. Subsequently, one obtains the $d = n \times \lambda_F/2$ values indicated. The black line is calculated for $U_0b = \infty$. The gap of data beyond $\lambda_F/2$ in Au corresponds to its faceting range. The inset is a blowout of the large-d region, where only Cu data are shown. The accuracy at this range does not allow to discard the hard wall case found in STM.

a terrace confinement effect ΔE plotted as a function of d for the three curved crystals. ΔE is a very convenient magnitude for ARPES studies of vicinal surfaces, because, unlike gaps, it is barely affected by the inherent terrace-size distribution broadening.[8] From ΔE one straightforwardly obtains the barrier strength within the simplest approach for a 1D superlattice, i.e., a periodic succession of δ-like barrier potentials of strength U_0b located at step edges. The δ barrier is equivalent to the finite potential barrier of height U_0 and width b depicted in Fig. 1(c), with the advantage of allowing the simple 1D KP analysis of the superlattice.[12] In the KP model, the 1D band dispersion is given by the known expression

$$E(k_x) = E_0 + \frac{\hbar^2}{2m^*}\frac{1}{d^2}[\cos^{-1}(|T|\cos k_x d) - \phi]^2, \qquad (2)$$

where m^* is the electron effective mass of the surface state and $|T|$ and ϕ are, respectively, the modulus and the phase of the energy-dependent, complex transmission coefficient.[12] Taking $k_x = 0$ and inserting the analytical expressions for $|T|$ and ϕ in Eq. (2), it immediately follows the terrace-size effect $\Delta E = E(0) - E_0$ as

$$\Delta E = \frac{2\hbar^2}{m^*}\frac{1}{d^2}\left[\tan^{-1}\left(\frac{q_0}{q}\right)\right]^2, \qquad (3)$$

where $q_0 = (m^*/\hbar^2) \times U_0b$ and $q = \sqrt{(2m^*/\hbar^2)\Delta E}$. Data points in Fig. 4 correspond to ΔE vs $(1/d)$ measured across the three crystals. The reference energies E_0 of the (111) planes, measured at $\alpha = 0°$, are -0.056 eV for Ag(111) (100 K), -0.408 eV for Cu(111) (180 K), and -0.464 eV for Au (150 K),[15] agreeing with the literature.[8,12–14] The lines in Fig. 4 represent fits to the data following Eq. (3), where we assume $m^* = 0.41m_e$ for both Cu and Ag, $m^* = 0.27m_e$ for Au,[9] and use U_0b as the single fitting parameter. For the three crystals, we find an extraordinary agreement with the KP model, proving the correctness of this approach despite its simplicity.

In Fig. 4 we note that a single value U_0b holds for each crystal at all d regimes, except in Au, where U_0b changes at both sides of the faceting region ($4° < \alpha < 10°$). The small 0.6 eV Å barrier for Ag steps was also suggested in Ag/Cu(111) experiments.[16] The $U_0b = 1.7$ eV Å value found for Cu contrasts with the large 7.0 eV Å strength claimed in Ref. 8. The systematic analysis of Fig. 4 discards such a large value. For Au and Cu, the present experiment allows us to refine the conclusions drawn from the latest data collection of flat samples.[13] U_0b was found to fall within a constant 1–2 eV Å range for $d < 40$ Å, in overall agreement with Fig. 4. However, earlier data for $d > 40$ Å suggested a sharp barrier increase for large terraces.[13] The inset in Fig. 4 is a zoomout of the large-d regime. The present $\Delta E(1/d)$ data fall away from the hard wall case ($U_0b = \infty$), although error bars indicate that the infinite barrier cannot be discarded for $d > 40$–50 Å.

The accurate determination of the barrier strength for Au, Cu, and Ag steps is very important in the understanding of electron scattering at surfaces, e.g., in novel topological surface states, for which noble-metal surfaces are the nontopological reference.[17] STM and ARPES measurements of the step barrier in noble metals have always appeared contradictory, revealing in fact complex underlying physics.[4–6,8,12,13,18] The analysis of standing-wave patterns formed around isolated steps indicate high reflectivity and partial leakage (absorption) into bulk states.[4–6] By contrast, dense arrays of steps always exhibited surface band dispersion and reduced d-size effects in ARPES,[12,13,19] as also observed in Figs. 2 and 3. This is only explainable with small barriers that allow significant electron transmission.

Scattering differences between arrays with low and high density of steps were traced to the smooth transformation of surface states of large (111) terraces into bulk resonances in densely stepped surfaces.[12,13,18,19] Although fluctuations and disorder of the step lattice in Cu,[14] or surface-state depopulation in Ag,[20] both occurring at $d = \lambda_F/2$, have been claimed to trigger the transition from surface states to surface resonances, such a transition may be expected naturally. In reciprocal space, owing to the effective vanishing of the supporting band gap out of the [111] direction,[12] and in real space, owing to resonance buildup by a surface-bulk state overlap at step edges,[18] which significantly extends inside terraces.[21] Hence, a complex bulk-surface nature characterizes electronic states in step arrays, such that the distinct sensitivity to bulk and surface may explain the differences observed between ARPES and STM. In this respect, ARPES accurately determines the whole k-dependent spectrum,[12,13] although it is affected by crystal imperfections and size distribution broadening that are avoided in STM.

One question that arises from Fig. 4 is why U_0b increases from Ag to Cu and to Au. The answer can shed new light on the nature of the step potential, a key issue that, to the best of our knowledge, has been barely discussed in the past.[12,22] It is generally assumed that $U_0 b$ is related to the local electrostatic dipole at the step edge,[21,22] although the effective barrier strength may depend on wave-function properties of the surface state.[12,22] Because the latter is similar in Ag, Cu, and Au, one may reasonably expect $U_0 b$ to scale with the step dipole moment. However, consistent data on dipole moments of steps for the three metals do not exist. There are only partial comparative measurements in surface-vacuum[23] or surface-electrolyte interfaces,[24] which point to the trend found for $U_0 b$ in Fig. 4, i.e., the step dipole in Au is found to be bigger than in Cu or Ag, and larger for A steps versus B steps.

Coming back to the issue of the structural-electronic interplay, electronic instabilities are expected at 1D nesting values $d = n \times \lambda_F/2$, for which superlattice gaps lie at E_F. Gaps are clear in Au ARPES data[9] and Cu (Fig. 2, Ref. 8), but are hardly visible in Ag (Fig. 3), as expected from its small $U_0 b$ barrier. In Fig. 4 we have marked the $d = n \times \lambda_F/2$ values determined from the 1D KP bands $E(k_x)$ calculated using the respective $U_0 b$ in Eq. (2). KP bands for Cu are shown superimposed onto ARPES data in Fig. 2(a), indicating overall good agreement. In Cu we obtain $\lambda_F/2 = 17$ Å and $\lambda_F = 32$ Å, for Ag, $\lambda_F/2 = 45$ Å, whereas in Au, $\lambda_F/2 = 20$ Å and $\lambda_F = 36$ Å. Note that λ_F in Au lies exactly at the lower faceting onset at $\alpha \sim 4^\circ$.[9] Faceting is not present in Ag or Cu, which show a gradual change in lattice constant, reflected in the smooth evolution of ΔE in Fig. 4. However, Cu in fact shows d-size distribution instabilities at $\lambda_F/2 < d < \lambda_F$, as discussed next.

IV. STM: ANALYSIS OF THE TERRACE WIDTH DISTRIBUTION

The curved surface approach allows a straightforward structural analysis of the step superlattice as a function of d, using STM. In Au, such an analysis allowed us to characterize the faceting transition (miscut range, and terrace and step structure) of the crystal, which in turn made it possible to establish a likely connection between the faceting instability and the electronic states at the $\alpha \sim 4^\circ$ onset.[9] In Cu and Ag we have not detected faceting instabilities. The images in the top panels of Fig. 5 exemplify the main STM observation, i.e., monatomic step arrays with sizable variations in lattice quality across the curved surface, which are accounted for by means of the terrace width distribution $\sigma(\bar{d})$ analysis. At certain d values (e.g., 23.5 Å) the step lattice looks sharp, whereas at others ($d = 18.7$ Å) the step edges appear rougher. This qualitative observation is reflected in the image analysis of the bottom panels, where we plot the statistical variation of d (in entire multiples of atomic rows) across the image. The Gaussian fit gives the mean terrace size $\bar{d}$, as well as the standard deviation σ in each case.

In Figs. 6(a) and 6(b) we plot the standard deviation σ as a function of the average terrace size $\bar{d}$ in Cu and Ag, as determined from the statistical analysis of STM images extended to the whole crystals. Within the framework of the classical elastic model, the $\sigma(\bar{d})$ plot is very meaningful. In such a classical theory, step interactions are assumed to be dipolelike, and hence described by an inverse square potential $U(x) = \tilde{A}/x^2$.[2,25] $\tilde{A}$ refers to the step-step interaction strength, which varies as $(\sigma/\bar{d})^{-4}$.[26] Thus, for constant $\tilde{A}$, there is a direct proportionality between $\bar{d}$ and σ, i.e., a linear $\sigma(\bar{d})$ plot reflects an elastically stable (constant $\tilde{A}$) step lattice.

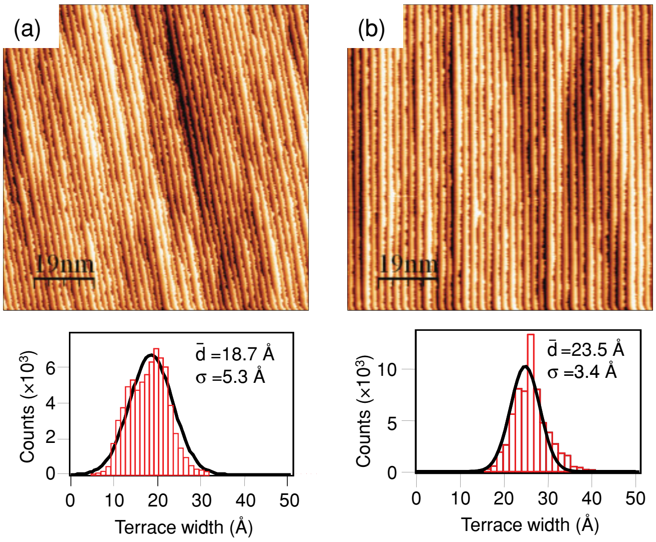

FIG. 5. (Color online) Characteristic STM images (top) from Cu curved surfaces showing (a) relatively broad (18.7 Å) and (b) sharp (23.5 Å) step lattices. The respective statistical image analysis (bottom) renders the average terrace size $\bar{d}$ and the standard deviation σ.

In Fig. 6, straight lines fit the A and B step data separately. In general, in both Cu and Ag, B data show larger scattering than A data, but the same trends. In Ag, within error bars, we observe a good linear fit, particularly in A steps. In contrast, Cu data deviate neatly from the line between $\lambda_F/2$ and λ_F, defining a dip with a minimum at $\bar{d} = 23$ Å. In fact, the step array is visually sharper in Fig. 5(a) for $\bar{d} = 23.5$ Å as compared to $\bar{d} = 18.7$ Å. By contrast to the Cu behavior, the data for Ag indicate, within error bars, an apparent stability, i.e., a constant $\tilde{A}$ value. Note that differences between Ag and Cu in $\sigma(\bar{d})$ plots correlate well with the respective superlattice potential derived from Fig. 4, i.e., weak for Ag and strong for Cu. In the following we try to discuss more quantitatively such a connection.

V. DISCUSSION: ELECTRONIC AND ELASTIC ENERGY INSTABILITIES

For a quantitative evaluation of any electronic-structural interplays, one must compare the characteristic energy variations involved at critical lattice constants, i.e., electronic ΔE_{elec} versus elastic ΔE_{elas}. In step arrays, these can be respectively estimated assuming the 1D KP band structure for the 1D lattice of Eq. (2) and the elastic theory.

The ΔE_{elec} is related to the presence of the superlattice gaps at E_F [Figs. 2(a) and 2(c)], which cause abrupt changes in the occupation of the surface band. To evaluate the surface-state occupation, we calculate numerically the number of electronic states per surface atom N_e by using the following formulas for

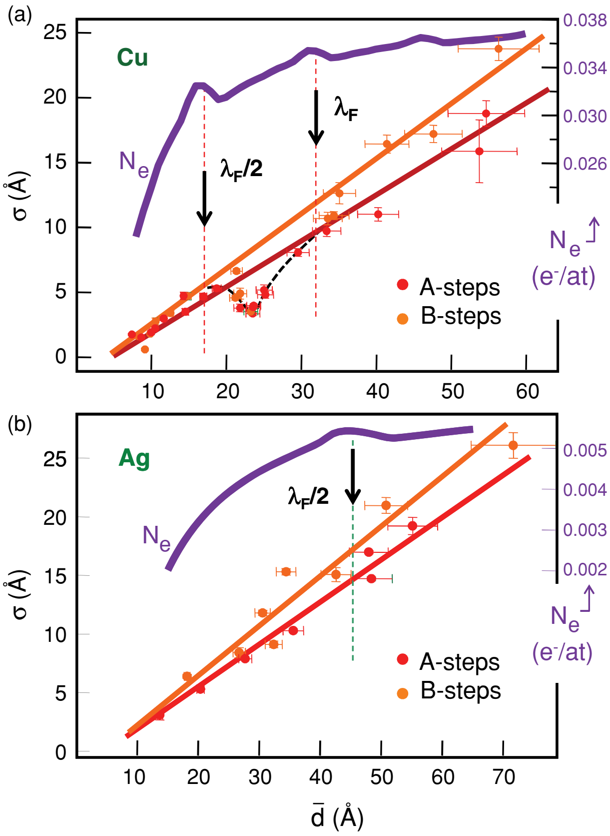

FIG. 6. (Color online) Terrace width variation σ as a function of the average lattice constant $\bar{d}$ for (a) Cu and (b) Ag, as determined with STM. A linear function is expected in lattices with inverse square $\tilde{A}/x^2$ step interactions but constant $\tilde{A}$ strength. Straight lines fit separately A and B step data in each crystal. For Cu, a dip (dotted line) is observed between $\lambda_F/2$ and λ_F, suggesting a structural instability triggered by surface states. The surface electron density curves shown on top are calculated with the KP model and the $U_0 b$ values of Fig. 2. They exhibit ripples at critical $n \times d = \lambda_F/2$ points.

2D systems:

$$D(\epsilon) = 2 \times \frac{1}{(2\pi)^2} \int_{E(k)=\mathrm{const}} \frac{dS_E}{|\mathrm{grad}_k E(k)|}, \qquad (4)$$

$$N_e = \int_{E_0}^{0} D(\epsilon) d\epsilon, \qquad (5)$$

where ϵ stands for the electron energy, $D(\epsilon)$ stands for the 2D density of states, and dS_E is an area element of the constant energy surface perpendicular to k. Equations (4) and (5) have been integrated numerically assuming, along k_x, the KP band structure of Eq. (2), and along k_y, a free-electron-like dispersion. In Fig. 6 we plot the resulting $N_e(d)$ curve on top of the $\sigma(\bar{d})$ plots. N_e increases steadily, but instabilities at successive gap crossings are clearly observed. In Cu we find $\Delta N_e \sim 0.001e^-$ ripples, whereas in Ag, owing to the smaller $U_0 b$ potential, ΔN_e is reduced to $\sim 0.0002e^-$/atom.

The corresponding variation in electronic energy ΔE_{elec} can be estimated following the criterium applied in Ref. 8, i.e., from the difference in electronic energy between gapped KP bands and gapless free-electron bands with constant occupation N_e. The total electronic energy per surface atom E_{elec} is derived from the known equation

$$E_{\mathrm{elec}} = \int_{E_0}^{0} \epsilon D(\epsilon) d\epsilon. \qquad (6)$$

The direct integration of Eq. (6) using the band structure of Eq. (2) results in the electronic energy for the KP lattice $E_{\mathrm{elec}}^{\mathrm{KP}}$. For the 2D free-electron gas, first we find the energy $\tilde{E}_0$ in Eq. (5) at which the electron density for KP bands and free-electron bands are strictly the same, $N_e^{\mathrm{KP}}(E_0) = N_e^{\mathrm{free}}(\tilde{E}_0)$. For such $\tilde{E}_0$ we integrate Eq. (6) to obtain $E_{\mathrm{elec}}^{\mathrm{free}}$. The electronic energy instability ΔE_{elec} is thus defined as

$$\Delta E_{\mathrm{elec}} = E_{\mathrm{elec}}^{\mathrm{free}}(\tilde{E}_0) - E_{\mathrm{elec}}^{\mathrm{KP}}(E_0). \qquad (7)$$

Applying Eqs. (4)–(7) around $\lambda_F/2$, we find $\Delta E_{\mathrm{elec}} \sim 0.3$ meV/atom in Cu in contrast to the much smaller $\Delta E_{\mathrm{elec}} \sim 0.005$ meV/atom found in Ag.

For ΔE_{elas} we consider the step interaction contribution to the surface free energy γ. In a vicinal surface with monatomic steps, γ can be expressed in terms of the miscut α and as a function of the temperature T:[2,25]

$$\gamma(\alpha) = \gamma_0 + \beta \frac{|\tan \alpha|}{h} + \frac{B(T)}{a_{||} h^3} |\tan \alpha|^3, \qquad (8)$$

where γ_0 represents the surface energy of (111) terraces, β is the step energy per unit length, h is the step height, $a_{||}$ is the atomic distance parallel to the steps, and $B(T)$ is the step interaction term. The latter includes both the entropic interaction $g(T)$, which is dominant at extremely low step densities, and the direct step-step interaction. For the specific case of step-step interactions of dipole type $U(x) = \tilde{A}/x^2$, $B(T)$ can be written as [2]

$$B(T) = \frac{g(T)}{4} \left\{ 1 + \left[1 + \frac{2\pi^2 \tilde{A} a_{||}}{3g(T)} \right]^{1/2} \right\}^2. \qquad (9)$$

For a moderate step density, which is the case of the 0°–15° miscut range analyzed in this work, $\tilde{A} > g(T)$, and $B(T)$ is reduced to

$$B(T) \simeq \frac{\pi^2 a_{||}}{6} \tilde{A}. \qquad (10)$$

In systems with faceting instabilities, such as Au,[9] two phases compete with their distinct terrace and step energies,[27] namely, the first and second terms in Eq. (8). In Cu and Ag we have a single phase, and hence lattice instabilities involve the third term of Eq. (8). Noting again that a constant interaction strength $\tilde{A}$ leads to a linear $\sigma(\bar{d})$ plot, the dip observed in Fig. 6 for Cu may be assumed as owing to $\Delta\tilde{A}$ changes, which in turn lead to elastic free-energy changes $\Delta\gamma = \Delta E_{\mathrm{elas}}$ as

$$\Delta E_{\mathrm{elas}} = \frac{\pi^2}{6h^3} |\tan \alpha|^3 \, \Delta\tilde{A} = \frac{\pi^2}{6d^3} \Delta\tilde{A}. \qquad (11)$$

The strong $(\sigma/\bar{d})^{-4}$ dependence of $\tilde{A}$ makes it difficult to obtain reliable $\tilde{A}$ values from STM data.[26] Among Cu(111) vicinals, $\sigma/\bar{d}$ is found close to 0.3, being $\tilde{A} \sim 6$ meV Å.[26] Assuming $\tilde{A} = 6$meV Å for $d = 17$ Å, the drop from $\sigma/\bar{d} = 0.28$ to $\sigma/\bar{d} = 0.14$ for $d = 23$ Å leads to an increase of $\tilde{A}$ to 96 meV Å. The latter value is typical for strongly interacting steps such as those in Pt(111).[25] Thus, around $\lambda_F/2$ for Cu in

Fig. 6, we estimate $\Delta\tilde{A} = 90$ meV Å, which results [Eq. (11), $d = 17$–23 Å] in $\Delta E_{\text{elas}} = 0.07$–$0.17$ meV/atom.

Therefore, based on the simple KP and elastic models, the same 0.1 meV/atom order of magnitude is estimated in Cu step lattices for electronic instabilities, caused by opening the gap at E_F, and elastic instabilities, caused by changes in step interaction strength. In the case of Ag, note that data in Fig. 6 exhibit the same slopes as in Cu, and hence it is reasonable to expect similar elastic energy variations upon similar $\tilde{A}$ changes. Thus, the small $\Delta E_{\text{elec}} = 0.005$ meV/atom involved in the Fermi gap crossing in Ag would not be sufficient to trigger a visible ΔE_{elas} instability in Fig. 6.

VI. SUMMARY

In summary, using curved crystals, we carried out a consistent surface-state and structure analysis of Ag, Cu, and Au step lattices with smoothly varying d, using ARPES and STM. With ARPES we measured the superlattice band structure and the terrace confinement effect as a function of d. From the latter, we accurately obtained the superlattice potential, which remains constant upon d variation, but increases from Ag to Cu and to Au. With STM we measured the d-size distribution in Cu and Ag. We detect step lattice instabilities in the case of Cu within the $\lambda_F/2 < d < \lambda_F$ range. The quantitative estimation of both lattice (terrace width) and electronic (Fermi energy gap) instabilities based on the classical elastic theory and the KP band structure give the same (0.1 meV/atom) order of magnitude in Cu, suggesting the presence of electronic-structural interplays. By contrast, the weak electron potential in Ag appears insufficient to promote instabilities in the step lattice, which in fact appears structurally stable in STM.

ACKNOWLEDGMENTS

This work was supported in part by the Spanish MICINN (MAT2007-63083), and the Basque Government (IT-257-07). The SRC is funded by the National Science Foundation (Grant No. DMR-0084402).

---

[1] V. Shchukin, N. N. Ledentsov, and D. Bimberg, *Epitaxy of Nanostructures*, Series on NanoScience and Technology, edited by Ph. Avouris, K. von Klitzing, H. Sakaki, and R. Wiesendanger, Vol. XII (Springer, Berlin, 2004).

[2] E. D. Williams and N. C. Bartelt, Science **251**, 393 (1991).

[3] M. Ternes, M. Pivetta, F. Patthey, and W.-D. Schneider, Prog. Surf. Sci. **85**, 1 (2010).

[4] M. F. Crommie, C. P. Lutz, and D. M. Eigler, Nature (London) **363**, 524 (1993).

[5] Y. Hasegawa and Ph. Avouris, Phys. Rev. Lett. **71**, 1071 (1993).

[6] L. Bürgi, O. Jeandupeux, A. Hirstein, and H. Brune, and K. Kern, Phys. Rev. Lett. **81**, 5370 (1998).

[7] F. Schiller, J. Cordón, D. Vyalikh, A. Rubio, and J. E. Ortega, Phys. Rev. Lett. **94**, 016103 (2005).

[8] F. Baumberger, M. Hengsberger, M. Muntwiler, M. Shi, J. Krempasky, L. Patthey, J. Osterwalder, and T. Greber, Phys. Rev. Lett. **92**, 016803 (2004).

[9] M. Corso, F. Schiller, L. Fernández, J. Cordón, and J. E. Ortega, J. Phys. Condens. Matter **21**, 353001 (2009).

[10] See supplemental material at [http://link.aps.org/supplemental/10.1103/PhysRevB.83.085411].

[11] I. Horcas, R. Fernández, J. M. Gómez Rodríguez, J. Colchero, J. Gómez-Herrero, and A. Baró, Rev. Sci. Instrum. **78**, 013705 (2007).

[12] A. Mugarza and J. E. Ortega, J. Phys. Condens. Matter **15**, S3281 (2003).

[13] A. Mugarza, F. Schiller, J. Kuntze, J. Cordón, M. Ruiz-Osés, and J. E. Ortega, J. Phys. Condens. Matter **18**, S27 (2006).

[14] F. Baumberger, M. Hengsberger, M. Muntwiler, M. Shi, J. Krempasky, L. Patthey, J. Osterwalder, and T. Greber, Phys. Rev. Lett. **92**, 196805 (2004).

[15] In Au, E_0 corresponds to the reconstructed (111) plane, and hence it may not be the appropriate reference at high miscuts. This was taken into account in a fit to the whole surface band (Ref. 9), but the $U_0 b$ values obtained were similar to those in Fig. 4.

[16] F. Schiller, M. Ruiz-Osés, J. Cordón, and J. E. Ortega, Phys. Rev. Lett. **95**, 066805 (2005).

[17] J. Seo, P. Roushan, H. Bidenkopf, Y. S. Hor, R. J. Cava, and A. Yazdani, Nature (London) **466**, 343 (2010).

[18] R. Eder and H. Winter, Phys. Rev. B **70**, 085413 (2004).

[19] M. Hansmann, J. I. Pascual, G. Ceballos, H.-P. Rust, and K. Horn, Phys. Rev. B **67**, 121409 (2003).

[20] K. Morgenstern, K. F. Braun, and K. H. Rieder, Phys. Rev. Lett. **89**, 226801 (2002).

[21] Ph. Avouris, I.-W. Lyo, and P. Molinàs-Mata, Chem. Phys. Lett. **240**, 423 (1995).

[22] L. C. Davis, M. P. Everson, R. C. Jaklevic, and W. Shen, Phys. Rev. B **43**, 3821 (1991).

[23] See M. Roth, M. Pickel, J. Wang, M. Weinelt, and Th. Fauster, Appl. Phys. B **74**, 661 (2002) and references therein.

[24] See G. Beltramo, H. Ibach, U. Linke, and M. Giesen, Electrochim. Acta **53**, 6818 (2008) and references therein.

[25] E. D. Williams, Surf. Sci. **299/300**, 502 (1994).

[26] M. Giesen, Prog. Surf. Sci. **68**, 1 (2001).

[27] S. Rousset, V. Repain, G. Baudot, Y. Garreau, and J. Lecoeur, J. Phys. Condens. Matter **15**, S3363 (2003).